

# Fast Non-Rigid Radiance Fields from Monocularized Data

Moritz Kappel<sup>1</sup> Vladislav Golyanik<sup>2</sup> Susana Castillo<sup>1</sup>  
 Christian Theobalt<sup>2</sup> Marcus Magnor<sup>1</sup>

<sup>1</sup> Computer Graphics Lab, TU Braunschweig, Germany {lastName}@cg.cs.tu-bs.de

<sup>2</sup> Max Planck Institute for Informatics, Saarland Informatics Campus, Germany {lastName}@mpi-inf.mpg.de



**Figure 1.** We introduce a new volumetric 3D scene reconstruction method for real-time novel view synthesis and temporal interpolation of non-rigidly deforming objects (left). It is trained on monocularized sequences, *i.e.* fixed single monocular frames per time-frame sampled from multi-view recordings (right). Our method enables fast optimization at a high visual accuracy in a just few minutes.

## Abstract

3D reconstruction and novel view synthesis of dynamic scenes from collections of single views recently gained increased attention. Existing work shows impressive results for synthetic setups and forward-facing real-world data, but is severely limited in the training speed and angular range for generating novel views. This paper addresses these limitations and proposes a new method for full 360° novel view synthesis of non-rigidly deforming scenes. At the core of our method are: 1) An efficient deformation module that decouples the processing of spatial and temporal information for acceleration at training and inference time; and 2) A static module representing the canonical scene as a fast hash-encoded neural radiance field. We evaluate the proposed approach on the established synthetic D-NeRF benchmark, that enables efficient reconstruction from a single monocular view per time-frame randomly sampled from a full hemisphere. We refer to this form of inputs as monocularized data. To prove its practicality for real-world scenarios, we recorded twelve challenging sequences with human actors by sampling single frames from

a synchronized multi-view rig. In both cases, our method is trained significantly faster than previous methods (minutes instead of days) while achieving higher visual accuracy for generated novel views. Our source code and data is available at our project page <https://graphics.tu-bs.de/publications/kappel2022fast>.

## 1. Introduction

The faithful reconstruction and rendering of non-rigidly deforming objects from a set of image or video captures is a longstanding challenge for a wide range of practical applications (*e.g.* creating virtual avatars for immersive AR/VR applications and movie production). Recent approaches build upon the success of neural radiance fields (NeRFs) [23], enhancing scene representation with an additional multilayer perceptron (MLP) that models temporal deformations in the recordings [33, 45, 30, 29]. Similar to static NeRF methods, these non-rigid extensions achieve an unprecedented visual quality for novel view synthesis. However, existing real-world datasets mostly comprise forward-facing scenes recorded by a moving monocu-

lar camera or multi-view camera grid, making it impossible to fully explore the reconstructed objects from the full angular range. Moreover, these methods also inherit the long training and inference times of NeRF, which even worsen due to the additional temporal dimension.

The D-NeRF approach by Pumarola *et al.* [33], on the other hand, provided a synthetic 360° inward-facing dataset, where position of a monocular camera is randomly resampled from a hemisphere for every time-frame. As this setup operates on a single monocular view at a time, but its practical implementation technically requires multiple synchronized cameras, we refer to it as *monocularized* data. In contrast to continuous camera trajectories (*e.g.* videos captured by a smartphone), this setup facilitates full 360° novel view synthesis at a high visual fidelity including complex motion, as the rapidly changing viewing angles for temporally coherent frames largely resolve the problem of occlusion and depth ambiguity. Despite criticism on its purely synthetic nature, the D-NeRF dataset was widely accepted by the community and is now frequently used as a benchmark for new approaches. The monocularization setup was already adapted for forward facing scenes recorded by a stereo camera setup, where the training images are alternately sampled from the left and right camera [29, 30]. However, the applicability to fast real-world full object reconstruction remains under-explored.

In response to the above-mentioned challenges, this paper introduces MoNeRF, *i.e.*, a new approach for 3D reconstruction and novel view synthesis of dynamic scenes from monocularized data; see Fig. 1. Our approach is general and works for arbitrary non-rigid objects. It takes a collection of monocular input images and foreground segmentation masks to reconstruct the depicted scene using a 4D deformation vector field that transforms spatiotemporal samples into a static, canonical radiance field representation. Our core finding is that a factorization between temporal and spatial domain results in an increased accuracy and allows for efficient training acceleration. Therefore, we propose a fast deformation component that estimates the deformation vector field by splitting temporal and spatial information into individual MLPs. Furthermore, we adapt the fast hash-encoding proposed by InstantNGP [24] for representing the scene in a canonical space, making our model several magnitudes faster than previous approaches.

To demonstrate the practical adaptability of monocularized data to real-world inward-facing scene reconstruction, we record a new multi-view dataset consisting of twelve challenging sequences with human performances, and keep one image per time stamp. We show that, despite the drastic reduction in the number of inputs (and thus the compute and memory requirements of full multi-view systems [17]), our approach still enables visually appealing novel view synthesis. On both synthetic and real data, it yields a superior qual-

ity according to several metrics and converges in less than seven minutes, *i.e.*, multiple magnitudes faster than other methods [33, 45]. Our dataset and code will be released for research purposes. In summary, our main contributions are:

- The first method for spatiotemporal novel view synthesis from monocularized sequences on the basis of InstantNPG [24], which is trained in under seven minutes and achieves real-time framerates during inference.
- A neural factorization-based deformation module splitting spatial and temporal information in two MLPs to improve the visual quality and accelerate training.
- A real monocularized dataset with twelve sequences of humans wearing different (including loose) garments and facial performances, enabling evaluation of fast 360° novel view synthesis on real dynamic scenes.

## 2. Related Work

NeRF [23] inspired a multitude of follow up works, that adapt and extend it (as well as differentiable volume rendering) for a variety of rendering tasks. Prominent extensions propose improvements for antialiasing [1], unstructured in-the-wild data [21, 35] and unbounded scenes [54]. Our method is mainly concerned with the fast non-rigid scene reconstruction [29, 33, 18, 45]. In the following, we briefly review previous work on acceleration and temporal extensions for NeRF. An extensive discussion of neural rendering techniques can be found in the report by Tewari *et al.* [44].

**Dynamic Scene Reconstruction and Rendering.** Traditional non-rigid reconstructing approaches apply dense structure from motion [10, 28, 41, 46, 16], shape-from-template [36, 26, 40, 14, 13], RGB-D inputs [42, 2] or even differentiable physics simulation [5] to jointly infer information about scene appearance and deformation. Due to the high visual quality and flexibility of NeRF, a large branch of methods focuses on extensions for non-rigidly deforming scenes. Some methods add the temporal dimension by modeling the scene as a 4D radiance field, and include regularizers such as motion consistency [6, 18], foreground-background decomposition [8, 49] and explicit depth priors [50] to resolve motion and depth ambiguities. Another family of methods model dynamic deformations as a 4D deformation vector field into a static (canonical) scene representation. Previous work further applied explicit rigidity estimation with explicit vector field divergence losses [45], per-frame appearance and deformation latent codes [29] and hyperplane slicing [30] to improve stability. Our method adopts the split of deformation field and canonical space, but focuses on the fast reconstruction of full hemisphere (inward-facing scenes). Thus, it is most closely related to the D-NeRF approach by Pumarola *et al.* [33], who introduced a synthetic monocularized dataset to reconstruct dynamic foreground objects. Our method, however, signifi-



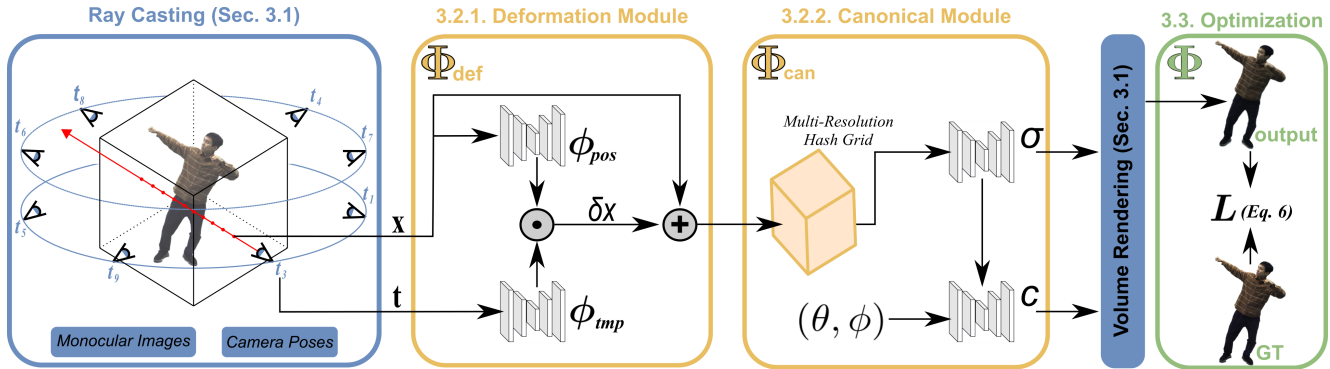


**Figure 2. Framework overview.** Our method takes a set of calibrated monocular RGBA images to reconstruct a deformable radiance field for novel-view synthesis. We feed sampled points  $x$  and their normalized timestamp  $t$  into individual shallow MLPs, and combine the resulting high-dimensional embeddings using matrix multiplication to obtain a deformation vector  $\delta x$  into canonical space. The canonical module is implemented as a fast hash-encoded neural radiance field, estimating opacity  $\sigma$  and view-dependent color  $c$  for volume rendering.

cantly accelerates training and improves the visual fidelity using a new factorization-based deformation module coupled with an explicit static scene representation. Furthermore, we demonstrate the practicability of our approach on real-world data on a new dataset generated by monocularizing inward-facing multi-view recordings (*i.e.* discarding all but one view per time-frame). In contrast to full multi-view methods for dynamic radiance fields reconstructing (*e.g.* using hyper spherical harmonics [53], Fourier transform [47] or compact latent codes [17]), our method and setup enable reconstruction in a matter of minutes due to the immense reduction in compute and memory requirements.

**NeRF Acceleration.** The training and rendering speed of conventional NeRF methods is often limited by the amount of ray-marching samples and expensive network queries during volume rendering. One branch of research focuses on improving inference times by applying efficient acceleration structures to the radiance field [9, 12, 34, 51], or introducing advanced ray sampling and stopping criteria [19, 32]. Another branch attempts to accelerate training using generalized pretrained models to fit novel scenes from one or few input views [52, 4, 20]. Recently, multiple works introduced explicit scene representations such as discrete grids [43, 37], to replace the costly MLP queries with efficient data lookups and trilinear interpolation. However, the reduced computational cost of dense data grids usually implies an increase in memory requirement, which can limit the obtainable rendering quality. To reduce the increased memory footprint, Chen *et al.* [3] model the explicit volume as a 4D tensor factorized into compact low-rank tensor components. Müller *et al.* [24] on the other hand propose an explicit feature encoding for MLP-based graphics primitives (including NeRFs) using multi-resolution hash grids. They work remarkably well on rigid scenes, but their adaptability for non-rigid extensions remains unclear. This work builds upon the success of instant NGP [24], introducing

the first approach leveraging hash encoding for non-rigid reconstruction from monocularized data.

**Concurrent Work on arXiv.** Concurrent to our work, other non-rigid NeRF methods for the monocularized setting adapt explicit scene representation to improve training and inference speed for inward-facing scenes. Guo *et al.* [11] adapt efficient direct voxel grid optimization [43] to model scene deformation, density and color. Fang *et al.* [11] use a time-aware neural voxel grid with multi-distance interpolation for fast, high-quality non-rigid reconstruction. For reference, we show that our hash-grid-based method trains faster while obtaining higher average scores according to several quality metrics on the D-NeRF benchmark dataset.

## 3. Method

Given a set of  $N$  calibrated input images  $I = (i_1, \dots, i_N)$  depicting a non-rigidly deforming object, the corresponding foreground masks  $S = (s_1, \dots, s_N)$ , and per frame-normalized timestamps  $T = (t_1, \dots, t_N) \in [0, 1]^N$ , our MoNeRF model enables joint novel view synthesis and seamless temporal interpolation in real time. As illustrated in Fig. 2, the core of our model comprises an explicit hashmap-based radiance field representing the scene in canonical (*i.e.* static undeformed) space, which is optimized using conventional neural volume rendering. We further incorporate temporal deformations in our model by pre-connecting an efficient ray-bending component transforming spatiotemporal samples into canonical space. In the following, we provide a detailed description of our individual framework components and the optimization procedure.

### 3.1. Volume Rendering

To optimize and render novel views from our model, we apply discrete sample-based ray marching derived from classical volume rendering [15] as introduced in the context

of NeRF [23]. As these fundamental concepts have been extensively discussed in the aforementioned literature, we provide a brief introduction of the mathematical concepts and notation necessary to delineate our method.

To query the expected color of a single pixel in a camera view  $n$ , we first construct a ray  $r(p) = o + pd$  starting at the camera’s optical center  $o$  and passing through the pixel’s center in direction  $d$ . For any continuous scene function  $\Phi$  (e.g., NeRF) mapping a spatial position  $x \in \mathbb{R}^3$  and viewing direction  $d \in \mathbb{R}^3$  to a density  $\sigma \in \mathbb{R}$  and color  $c \in \mathbb{R}^3$ , i.e.,

$$(\sigma, c) = \Phi(x, d), \quad (1)$$

we can then evaluate the local scene properties  $(\sigma_i, c_i)$ ,  $i \in \{1, \dots, M\}$  for a set of  $M$  discrete spatial samples  $x_i = (r(p_i), p_i \sim [p_n, p_f])$  along the ray within a predefined minimal ( $p_n$ ) and maximal ( $p_f$ ) distance from the image plane. The final pixel color is obtained by estimating the integral  $C(r)$  over all samples according to the optical model of Max [22]:

$$C(r) = \sum_{i=1}^M T_i (1 - \exp(-\sigma_i \delta_i)) c_i, \quad (2)$$

where  $T_i = \exp(-\sum_{j=1}^{i-1} \sigma_j \delta_j)$  and  $\delta_i = p_{i+1} - p_i$  denotes the distance between adjacent samples. Finally, we use the pixel’s total transmittance  $\alpha(r)$  given by

$$\alpha(r) = \sum_{i=1}^M T_i (1 - \exp(-\sigma_i \delta_i)) \quad (3)$$

to blend the estimated color with a static background color.

The following section describes how our method represents the local scene density and color for rendering non-rigid scenes.

## 3.2. Scene Representation

The scene function (Eq. 1) has no notion of time, and thus cannot reflect objects undergoing non-rigid deformations. Inspired by previous work on deforming radiance fields [33, 45], we introduce a framework consisting of two distinct subcomponents to handle the temporal dimension: A static module  $\Phi_{\text{can}}$  representing the scene in canonical (i.e. undeformed) space, and a deformation module  $\Phi_{\text{def}}$  estimating the offset of a spatial point at timestamp  $t$  into its canonical state. Formally, the full scene function implemented in our framework can be rewritten as:

$$\Phi(x, d, t) = \Phi_{\text{can}}(x + \Phi_{\text{def}}(x, t), d). \quad (4)$$

### 3.2.1 Deformation Module

The deformation module  $\Phi_{\text{def}}$  estimates the deformation vector  $\delta x \in \mathbb{R}^3$  for a discrete spatial position  $x$  at a normalized timestamp  $t$ . This process was previously described as

a form of ray bending, where rays cast by a virtual video camera are distorted so that related samples along the rays can be evaluated at their original location in a canonical volume [45]. Recent methods usually implement ray bending using a single multilayer perceptron (MLP) of a similar size as the canonical NeRF itself [33, 45, 29]. While this approach can represent high-quality deformation fields, it also significantly contributes to the overall computational cost, both during training and inference. To reduce execution times while preserving high quality, we propose a new deformation module architecture decoupling the processing of spatial and temporal information into individual MLPs:

$$\delta x = \Phi_{\text{def}}(x, t) = \phi_{\text{pos}}(x) \odot \phi_{\text{tmp}}(t), \quad (5)$$

with  $\phi_{\text{pos}} : \mathbb{R}^3 \rightarrow \mathbb{R}^{3 \times l}$  denoting the positional MLP,  $\phi_{\text{tmp}} : \mathbb{R} \rightarrow \mathbb{R}^{l \times 1}$  denoting the temporal MLP, and  $\odot$  being conventional matrix multiplication. We further apply frequency encoding [23] to the input position and one-blob encoding [25] to the timestamp before passing them to the neural networks to enable higher frequencies.

The key idea of our approach is disentanglement of the embeddings into temporal and spatial components. Thus, we estimate a higher-dimensional feature vector of size  $l$  for every spatial input dimension, which is then reduced to a single offset by linear combination with temporally varying coefficients (estimated by a separate network). With sufficient capacity, i.e., a large enough  $l$ , this representation can support arbitrary deformation fields and does not limit the overall model expressivity. As a result, this policy enables the use of more shallow network architectures with fewer input parameters; it accelerates training while maintaining an overall high quality of the deformation field. The speed up is particularly noticeable when querying deformation vectors for the same spatial positions over multiple points in time, as the positional MLP  $\phi_{\text{pos}}$  needs to be executed only once. Temporal basis vectors can be inferred and applied in parallel, allowing for efficient acceleration strategies as described in Sec. 3.4.

### 3.2.2 Canonical Module

After shifting the input samples to the canonical space by adding the estimated offset  $\delta x$ , we apply a static radiance field representation  $\Phi_{\text{can}}$  to obtain their local density  $\sigma$  and view-dependent color values  $c$  as stated earlier in Eq. (1). For this purpose, we adapt the recent instant neural geometric primitives (NGP) introduced by Müller *et al.* [24], which reconstructs NeRF in a few minutes at a competitive visual quality. The authors achieve this unprecedented level of speed by replacing the frequency-based input encoding [23] with an explicit multi-resolution hash grid encoding. For our framework, we apply a fast PyTorch [31] implementation using the architectural hyperparameters provided in the original publication.

### 3.3. Optimization

We optimize our full model  $\Phi$  (Eq. 4) end-to-end over the course of  $30k$  training iterations via stochastic gradient descent. During each iteration, we chose a random camera view  $n \in \{1, \dots, N\}$  with associated image  $i_n$ , foreground mask  $s_n$ , and timestamp  $t_n$ . For this view, we uniformly sample a batch  $R$  of 8192 rays, which are rendered using a maximum of 512 samples per ray.

Our full objective function  $L$  consists of three terms:

$$L = L_{\text{photo}} + \lambda_{\text{bg}} L_{\text{bg}} + \lambda_{\text{def}} L_{\text{def}}, \quad (6)$$

with scalar hyperparameters  $\lambda_{\text{bg}}$  and  $\lambda_{\text{def}}$  that we set to  $10^{-2}$  and  $10^{-3}$  for all our experiments, respectively. The photometric loss  $L_{\text{photo}}$  compares the estimated pixel color  $c_{\text{estim}}$  to the ground truth pixel color  $c_{\text{gt}}$ :

$$L_{\text{photo}} = \frac{1}{|R|} \sum_{r \in R} \|C(r) - C_{\text{gt}}(r)\|_2^2, \quad (7)$$

where  $C_{\text{gt}}(r)$  denotes the ground-truth color of ray  $r$  in the training view  $i_n$ . Following Müller *et al.* [24], we stabilize training by applying a random background color during each iteration based on the ray transmittance  $\alpha(r)$  and foreground mask  $s_n$  for the estimated and ground-truth color respectively. We further apply two regularization losses to stabilize the optimization and improve the generalization to novel views. The background entropy loss  $L_{\text{bg}}$  enforces a clear transition between foreground object and empty scene space, while the deformation field regularizer  $L_{\text{def}}$  encourages the deformations to small and sparse:

$$L_{\text{bg}} = \frac{1}{|R|} \sum_{r \in R} -\alpha_r \log(\alpha_r), \quad (8)$$

$$L_{\text{def}} = \frac{1}{|X_\delta|} \sum_{\delta x \in X_\delta} \|\delta x\|_1. \quad (9)$$

Here,  $X_\delta$  denotes the set of all deformation vectors estimated via Eq. (4) during rendering. The entire optimization takes 6-7 minutes on a single NVIDIA RTX 3090 GPU. Our full implementation is available on our project page.

### 3.4. Acceleration Strategies

An advantage of our method is that—despite adding a temporal extension to the radiance field—we can directly apply the ray marching acceleration techniques proposed for instant NeRF, such as transmittance-based stopping criteria to speed up training and inference times [24]. Another common way to increase inference speed is keeping track of an occupancy grid, which marks unoccupied (empty) scene space that can be skipped during ray marching [24, 43]. However, naively applying an occupancy grid to our canonical module implies that the deformation module needs to

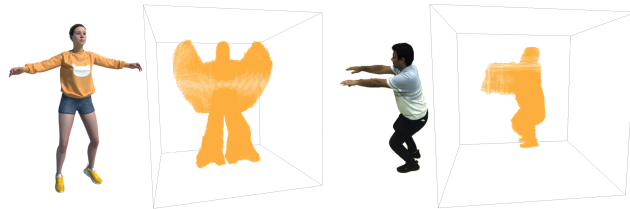


**Figure 3. A point cloud visualization of our temporal occupancy grids.** Left: A synthetic human avatar performing jumping jacks. Right: A real recording of an actor performing squats.

be executed for all samples before being able to skip single evaluations in canonical space, which would result in a significant performance loss. Thus, we extend this acceleration structure in the form of a temporal occupancy grid, which marks points in space that are occupied during any timestamp in the normalized time period  $[0, 1]$ , as visualized in Fig. 3. This way, both the canonical and deformation module are only evaluated on a sparse subset of the scene to model the foreground object and resolve the (dis)occluded areas. We can then update our temporal grid by sampling a set of candidate cells as proposed by Müller *et al.* [24] for the rigid case, and threshold the accumulated density from a set of  $l$  random equidistant timestamps. For all our experiments, we use  $q = 20$  temporal samples, which can efficiently be evaluated in parallel by our deformation model.

## 4. Monocularized Multi-View Actors Dataset

To investigate the applicability of the monocularized data setup for real-world inward-facing scenes, we record new sequences in the spirit of the synthetic D-NeRF [33] dataset. We dub our novel real-world dataset Monocularized Multi-View Avatars (MMVA). It comprises a total of 12 sequences showing a variety of actors and clothing (10 full body and 2 faces) performing a single motion, captured by a large inward-facing multi-view setup of up to 112 synchronized 50Hz cameras. Each sequence consists of  $n \in [100, 250]$  RGB images with a resolution of  $1028 \times 752$  pixels, and the corresponding foreground masks obtained via background subtraction. We monocularize the multi-view recordings by randomly extracting a single image per time-frame from a uniformly sampled camera, resulting in a total of  $n$  training images with temporally varying camera positions and viewing directions. During training image sampling, we leave out two expressive camera views which we reserve for the test and validation sets.

Discarding a significant percentage of training data implies an inevitable loss in the accessible reconstruction quality. However, as evident by the synthetic D-NeRF dataset, monocularized data is compact in size ( $\sim 500\text{MB}$  per sequence for our MMVA dataset) and thus drastically reduces the compute and memory requirement of full multi-view

		D-NeRF Dataset					
		PSNR $\uparrow$	SSIM $\uparrow$	LPIPS $\downarrow$	Time	Storage	
STATIC	NeRF [23]	19.00	0.87	0.18	$\sim$ hours	5 MB	
	DirectVoxGO [43]	18.61	0.85	0.17	5 mins	205 MB	
	Plenoxels [37]	20.24	0.87	0.16	6 mins	717 MB	
	InstantNGP [24]	19.00	0.88	0.17	5 mins	35 MB	
DYNAMIC	T-NeRF [33]	29.51	0.95	0.08	$\sim$ hours	n/a	
	D-NeRF [33]	30.50	0.95	0.07	$\sim$ hours	13 MB	
	NR-NeRF [45]	26.15	0.95	0.09	$\sim$ hours	13 MB	
	MoNeRF (ours)	<b>32.16</b>	<b>0.98</b>	<b>0.03</b>	7 mins	80 MB	
	TiNeuVox-S [7]	30.75	0.96	0.07	8 mins	8 MB	
	TiNeuVox-B [7]	32.67	0.97	0.04	28 mins	48 MB	
	NDVG [11]	30.32	0.96	0.05	20 mins	n/a	

**Table 1. Quantitative comparison on the D-NeRF Dataset [33].** The reported values are averaged over all eight sequences.

systems [17]. We show that MoNeRF can exploit those characteristics to perform fast NeRF reconstruction in minutes, while maintaining high visual quality for novel view synthesis. In the future, our dataset can help to further investigate the D-NeRF setup for practical applications (*e.g.*, in the context of integrated systems with memory and compute limitations, or to generate fast previews of recordings before applying expensive multi-view reconstruction). To this end, our dataset will be made publicly available.

## 5. Experimental Evaluation

We perform extensive experiments on an established synthetic dataset and the newly recorded real-world MMVA sequences. For quantitative and qualitative evaluation, we compare our MoNeRF to the most related state-of-the-art (SotA) methods, *i.e.*, D-NeRF [33], NR-NeRF [45], and the static InstantNGP [24]. We report three metrics for quantitative assessment: Peak signal-to-noise ratio (PSNR), structural similarity (SSIM) [48] and learned perceptual image patch similarity (LPIPS) [55]. While PSNR reflects the per-pixel error and is thus closest to the training objective function, SSIM and LPIPS gauge the perceptual reconstruction accuracy from a larger context. The video and additional visualizations are available in our supplement.

### 5.1. Synthetic Scenes

We use the D-NeRF dataset [33] to test and compare our method on clean synthetic data. It comprises eight sequences, each consisting of 50–200 frames, showing deforming objects of varying motion complexity. Similar to previous work, we downsample the images to half resolution ( $400 \times 400$  pixels) to fairly compare against other methods. Tab. 1 shows average quantitative results over all eight sequences, including training time and storage cost (see the supplement for a more detailed version). In addition to the abovementioned benchmark methods, we show results for further methods gathered from literature, including fast static radiance field methods [23, 43, 37, 24] and works

		MMVA Dataset		
		PSNR $\uparrow$	SSIM $\uparrow$	LPIPS $\downarrow$
	InstantNGP [24]	16.04	0.90	0.30
	D-NeRF [33]	31.77	0.97	0.07
	NR-NeRF [45]	29.84	0.97	0.04
	MoNeRF (ours)	<b>33.29</b>	<b>0.98</b>	<b>0.03</b>

**Table 2. Quantitative comparison on our MMVA Dataset.** We report the averages according to PSNR/SSIM (higher is better) and LPIPS (lower is better) on the set of 12 recorded scenes.

on arXiv [7, 11]. Compared to previous dynamic NeRF approaches [33, 45] that take  $\sim 20$  hours to reconstruct a single scene, our novel deformation network and explicit hash-encoded scene representation achieve significant improvements in the training speed (finishing training in under seven minutes and rendering novel views in real time). The quality metrics show that our approach also outperforms previous work in image quality, maintaining fine details in high-frequency areas, as shown in Fig. 4. Even compared to concurrent work, MoNeRF is faster and achieves the best overall trade-off between training speed and final image quality. Fig. 5 provides detailed evidence of model convergence. MoNeRF needs a fraction of the training iterations compared to other methods and yields detailed novel views in as few as  $30k$  update steps.

### 5.2. Real-World Scenes

We examine the effectiveness of our approach on real-world data by performing quantitative and qualitative evaluations on our new MMVA dataset (introduced in Sec. 4). In contrast to the tests with synthetic data, we train all methods at full resolution of  $1028 \times 752$  pixels. Fig. 6 shows results for MoNeRF and related benchmark methods on a variety of sequences featuring challenging non-rigid deformations and texture patterns. As evident from the qualitative evaluation—despite unavoidable uncertainties arising from camera calibration, synchronization and foreground extraction—monocularized data can effectively be applied for fast, high-fidelity non-rigid reconstruction in real-world scenarios. Moreover, our method again outperforms recent approaches both in image quality and training speed (see Tab. 2). Similar to the synthetic data, MoNeRF reconstructs finer, more detailed object surfaces and smoother motion in only seven minutes of training, without any adjustments or overhead for real-world recordings.

### 5.3. Ablation Study

We next study the impact of individual MoNeRF components. First, we investigate the significance of our deformation module factorization for the disentanglement of spatial and temporal information (Sec. 3.2.1). To this end, we train an alternative version of MoNeRF that directly infers point-wise offset vectors from 4D spatiotemporal input samples



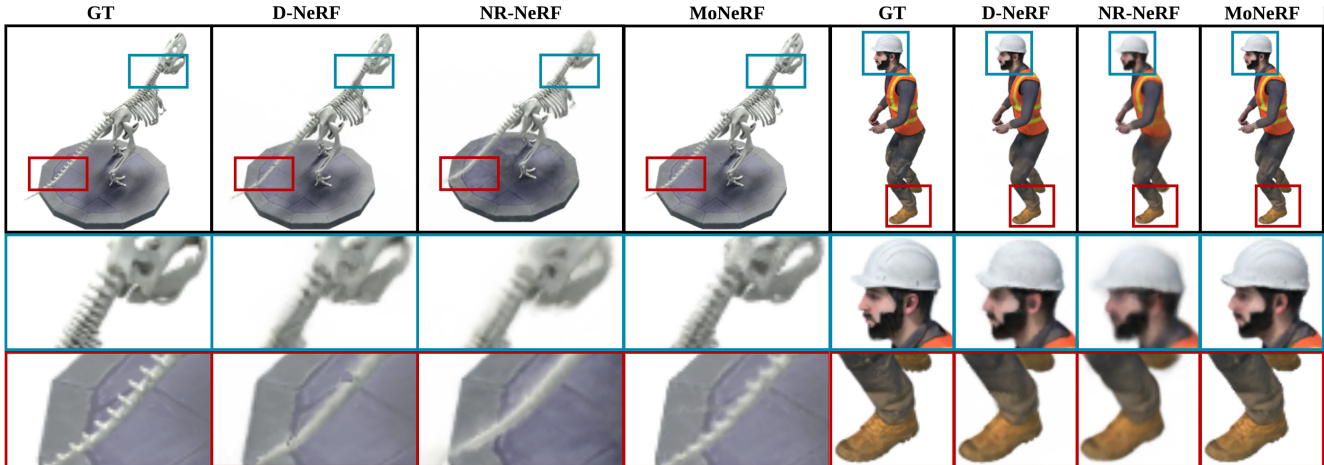


Figure 4. Comparison on the synthetic D-NeRF dataset [33]. We show detailed comparisons of our results (MoNeRF) against ground truth (GT) and benchmark methods for the *T-Rex* and *Stand Up* sequences.

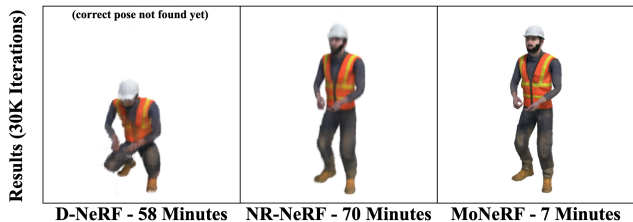
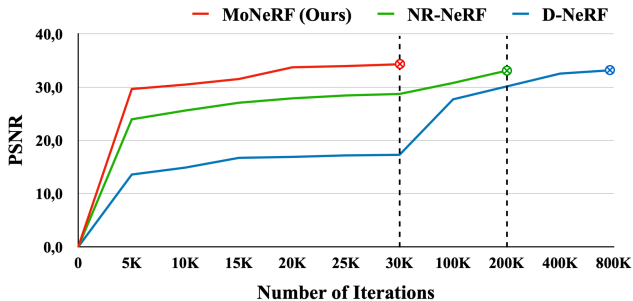


Figure 5. Comparison of training speed. (Top): The number of training iterations in relation to the test set PSNR on a synthetic sequence. (Bottom): An exemplary rendering and training time after 30k iterations. At this stage, NR-NeRF still produces blurry results and D-NeRF cannot yet portray the correct pose, while our MoNeRF displays fine texture and motion details.

in a single MLP with the same total amount of hidden layers. Moreover, we experiment with the number of temporal samples  $q$  used for approximating the temporal occupancy grid (Sec. 3.4), which is an essential component for training acceleration. Tab. 3 shows training times and average PSNR on the D-NeRF dataset for different configurations. We observe that our novel factorization-based deformation module achieves higher visual quality and enables faster occupancy grid updates (and thus overall training times) for larger  $q$  values, which are needed to retain delicate scene ap-

Temporal samples ( $q$ )	Factorization	PSNR $\uparrow$	Training Time $\downarrow$	$L_{bg}$ Eq. (8)	$L_{def}$ Eq. (9)	PSNR $\uparrow$
1	✓	31.88	4m 01s	✗	✗	31.35
1	✗	31.55	3m 57s	✗	✓	32.07
20	✓	32.16	6m 13s	✓	✗	31.52
20	✗	31.62	8m 18s	✓	✓	32.16
30	✓	32.23	7m 15s	-	-	-
30	✗	31.85	10m 27s	-	-	-

Table 3. Ablation experiment on the effect of our deformation module factorization, the number of samples  $q$  for updating the temporal occupancy grid, and the regularization losses. The highlighted rows show our final configuration.

pearance. Note that for  $q > 30$ , most GPUs run out of memory for parallel execution, resulting in a significant drop in performance without notably improving the reconstruction quality. We also assess the influence of our regularization losses and observe that both losses contribute to the overall accuracy (visually and in terms of average PSNR). The best results are obtained using our full objective function.

## 6. Discussion

Although MoNeRF achieves a superior visual quality compared to previous methods, it can still suffer from artifacts (*e.g.*, pixelation in areas undergoing fast motion). We assume that these effects are caused by the explicit nature of the underlying hash-grid representation, which does not offer the natural continuous regularization of large MLPs. We observe a similar effect on sequences recorded as a continuous camera trajectory (see Fig. 7): Despite its design for monocularized inward-facing setups, we test our method on a publicly available training sequence by Tretschk *et al.* [45]. While MoNeRF preserves finer geometric details, the generalization of motion to far off camera views is cur-



**Figure 6. Comparison on our MMVA dataset.** We compare our results (MoNeRF) against ground-truth (GT) and benchmark methods on a variety of real-world sequences comprising complex textures and motion. Note that MoNeRF produces sharper renderings and finer details than other methods (e.g., garment wrinkles, textures and the plush toy).

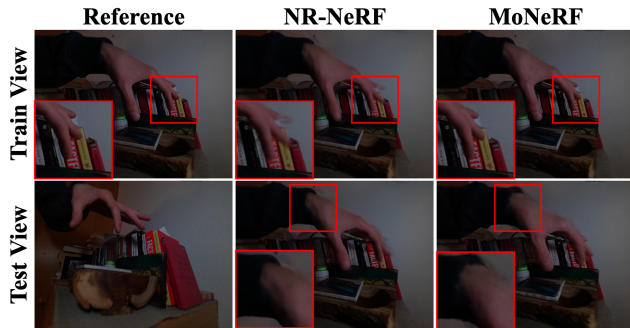


**Figure 7. Comparison on continuous training data.** We train our model on a continuous sequence provided by NR-NeRF [45], and render the video from a static camera position. (Top): The timestamp matching the camera position during training. (Bottom): A timestamp that was not observed from this camera position.

rently limited. In the future, adding explicit spatial and temporal regularizer can help to adjust our method for continuous monocular video and forward-facing scenarios.

Our experiments further demonstrate the effectiveness of monocularized real-world data. For future work, the investigation of more sophisticated importance sampling tech-

niques [27] on ray- or image-level is needed to optimize the setting for practical applications.

## 7. Conclusion

We introduced an unprecedentedly fast and accurate method for novel view synthesis of arbitrary non-rigidly deforming scenes in a monocularized setting. The win-win combination of fast training (inference) and accurate novel view synthesis is enabled by the new deformation module with separate spatial and temporal components. The experiments show that MoNeRF can reconstruct qualitatively appealing radiance and (temporally coherent) deformation fields for challenging scenes with fine appearance details in a matter of minutes, *i.e.*, several magnitudes faster than previous approaches. Moreover, we observe in the tests with our new dataset that the advantages of the proposed approach and monocularized setting can directly be transferred to real-world recordings. We believe our work opens many opportunities for applications and further research.

**Our supplementary material** contains additional details on our new dataset, and in depth comparisons with other techniques. The full implementation is available at our project page <https://graphics.tu-bs.de/publications/kappel2022fast>.

**Acknowledgements:** This work was partially funded by the DFG (MA2555/15-1 “Immersive Digital Reality”) and the ERC Consolidator Grant 4DRepLy (770784). We thank Timon Scholz, Basavaraj R Sunagad, and Kamuni Pranay Raj for helping with data recording and comparisons.

## References

- [1] Jonathan T Barron, Ben Mildenhall, Matthew Tancik, Peter Hedman, Ricardo Martin-Brualla, and Pratul P Srinivasan. Mip-nerf: A multiscale representation for anti-aliasing neural radiance fields. In *ICCV*, pages 5855–5864, 2021.
- [2] Aljaz Bozic, Pablo Palafox, Michael Zollhofer, Justus Thies, Angela Dai, and Matthias Nießner. Neural deformation graphs for globally-consistent non-rigid reconstruction. In *CVPR*, pages 1450–1459, 2021.
- [3] Anpei Chen, Zexiang Xu, Andreas Geiger, Jingyi Yu, and Hao Su. Tensorf: Tensorial radiance fields. In *ECCV*, 2022.
- [4] Anpei Chen, Zexiang Xu, Fuqiang Zhao, Xiaoshuai Zhang, Fanbo Xiang, Jingyi Yu, and Hao Su. Mvsnerf: Fast generalizable radiance field reconstruction from multi-view stereo. In *ICCV*, pages 14124–14133, 2021.
- [5] Hsiao-yu Chen, Edith Treitschk, Tuur Stuyck, Petr Kadlec, Ladislav Kavan, Etienne Vouga, and Christoph Lassner. Virtual elastic objects. In *CVPR*, pages 15827–15837, 2022.
- [6] Yilun Du, Yinan Zhang, Hong-Xing Yu, Joshua B Tenenbaum, and Jiajun Wu. Neural radiance flow for 4d view synthesis and video processing. In *ICCV*, pages 14304–14314. IEEE Computer Society, 2021.
- [7] Jiemin Fang, Taoran Yi, Xinggang Wang, Lingxi Xie, Xiaopeng Zhang, Wenyu Liu, Matthias Nießner, and Qi Tian. Fast dynamic radiance fields with time-aware neural voxels. *arXiv preprint arXiv:2205.15285*, 2022.
- [8] Chen Gao, Ayush Saraf, Johannes Kopf, and Jia-Bin Huang. Dynamic view synthesis from dynamic monocular video. In *ICCV*, pages 5712–5721, 2021.
- [9] Stephan J Garbin, Marek Kowalski, Matthew Johnson, Jamie Shotton, and Julien Valentin. FastNeRF: High-fidelity neural rendering at 200fps. In *ICCV*, pages 14346–14355, 2021.
- [10] Ravi Garg, Anastasios Roussos, and Lourdes Agapito. Dense variational reconstruction of non-rigid surfaces from monocular video. In *CVPR*, 2013.
- [11] Xiang Guo, Guanying Chen, Yuchao Dai, Xiaoqing Ye, Jiadai Sun, Xiao Tan, and Errui Ding. Neural deformable voxel grid for fast optimization of dynamic view synthesis. *arXiv preprint arXiv:2206.07698*, 2022.
- [12] Peter Hedman, Pratul P Srinivasan, Ben Mildenhall, Jonathan T Barron, and Paul Debevec. Baking neural radiance fields for real-time view synthesis. In *ICCV*, pages 5875–5884, 2021.
- [13] Erik Johnson, Marc Habermann, Soshi Shimada, Vladislav Golyanik, and Christian Theobalt. Unbiased 4d: Monocular 4d reconstruction with a neural deformation model. *arXiv preprint arXiv:2206.08368*, 2022.
- [14] Navami Kairanda, Edith Treitschk, Mohamed Elgharib, Christian Theobalt, and Vladislav Golyanik.  $\phi$ -sft: Shape-from-template with a physics-based deformation model. In *CVPR*, 2022.
- [15] James T Kajiya and Brian P Von Herzen. Ray tracing volume densities. *SIGGRAPH*, 18(3):165–174, 1984.
- [16] Suryansh Kumar and Luc Van Gool. Organic priors in non-rigid structure from motion. In *ECCV*, 2022.
- [17] Tianye Li, Mira Slavcheva, Michael Zollhofer, Simon Green, Christoph Lassner, Changil Kim, Tanner Schmidt, Steven Lovegrove, Michael Goesele, Richard Newcombe, et al. Neural 3d video synthesis from multi-view video. In *CVPR*, pages 5521–5531, 2022.
- [18] Zhengqi Li, Simon Niklaus, Noah Snavely, and Oliver Wang. Neural scene flow fields for space-time view synthesis of dynamic scenes. In *CVPR*, pages 6498–6508, 2021.
- [19] David B Lindell, Julien NP Martel, and Gordon Wetzstein. Autoint: Automatic integration for fast neural volume rendering. In *CVPR*, pages 14556–14565, 2021.
- [20] Yuan Liu, Sida Peng, Lingjie Liu, Qianqian Wang, Peng Wang, Christian Theobalt, Xiaowei Zhou, and Wenping Wang. Neural rays for occlusion-aware image-based rendering. In *CVPR*, pages 7824–7833, 2022.
- [21] Ricardo Martin-Brualla, Noha Radwan, Mehdi S. M. Sajjadi, Jonathan T. Barron, Alexey Dosovitskiy, and Daniel Duckworth. NeRF in the Wild: Neural Radiance Fields for Unconstrained Photo Collections. In *CVPR*, 2021.
- [22] Nelson Max. Optical models for direct volume rendering. *IEEE TVCG*, 1(2):99–108, 1995.
- [23] Ben Mildenhall, Pratul P. Srinivasan, Matthew Tancik, Jonathan T. Barron, Ravi Ramamoorthi, and Ren Ng. Nerf: Representing scenes as neural radiance fields for view synthesis. In *ECCV*, 2020.
- [24] Thomas Müller, Alex Evans, Christoph Schied, and Alexander Keller. Instant neural graphics primitives with a multiresolution hash encoding. *ACM TOG*, 41(4):102:1–102:15, July 2022.
- [25] Thomas Müller, Brian McWilliams, Fabrice Rousselle, Markus Gross, and Jan Novák. Neural importance sampling. *ACM TOG*, 38(5):1–19, 2019.
- [26] Dat Tien Ngo, Sanghyuk Park, Anne Jorstad, Alberto Crivellaro, Chang D. Yoo, and Pascal Fua. Dense image registration and deformable surface reconstruction in presence of occlusions and minimal texture. In *ICCV*, 2015.
- [27] Xuran Pan, Zihang Lai, Shiji Song, and Gao Huang. Activenerf: Learning where to see with uncertainty estimation. In *ECCV*, pages 230–246. Springer, 2022.
- [28] Shaifali Parashar, Mathieu Salzmann, and Pascal Fua. Local non-rigid structure-from-motion from diffeomorphic mappings. In *CVPR*, 2020.
- [29] Keunhong Park, Utkarsh Sinha, Jonathan T Barron, Sofien Bouaziz, Dan B Goldman, Steven M Seitz, and Ricardo Martin-Brualla. Nerfies: Deformable neural radiance fields. In *ICCV*, pages 5865–5874, 2021.
- [30] Keunhong Park, Utkarsh Sinha, Peter Hedman, Jonathan T. Barron, Sofien Bouaziz, Dan B Goldman, Ricardo Martin-Brualla, and Steven M. Seitz. Hypernerf: A higher-dimensional representation for topologically varying neural radiance fields. *ACM TOG*, 40(6), dec 2021.
- [31] Adam Paszke, Sam Gross, Francisco Massa, Adam Lerer, James Bradbury, Gregory Chanan, Trevor Killeen, Zeming Lin, Natalia Gimelshein, Luca Antiga, et al. Pytorch:

- An imperative style, high-performance deep learning library. *NeurIPS*, 32, 2019.
- [32] Martin Píala and Ronald Clark. Terminerf: Ray termination prediction for efficient neural rendering. In *3DV*, pages 1106–1114. IEEE, 2021.
- [33] Albert Pumarola, Enric Corona, Gerard Pons-Moll, and Francesc Moreno-Noguer. D-nerf: Neural radiance fields for dynamic scenes. In *CVPR*, pages 10318–10327, 2021.
- [34] Christian Reiser, Songyou Peng, Yiyi Liao, and Andreas Geiger. Kilonerf: Speeding up neural radiance fields with thousands of tiny mlps. In *ICCV*, pages 14335–14345, 2021.
- [35] Viktor Rudnev, Mohamed Elgharib, William Smith, Lingjie Liu, Vladislav Golyanik, and Christian Theobalt. Nerf for outdoor scene relighting. In *ECCV*, 2022.
- [36] Mathieu Salzmann, Julien Pilet, Slobodan Ilic, and Pascal Fua. Surface deformation models for nonrigid 3d shape recovery. *IEEE TPAMI*, 2007.
- [37] Sara Fridovich-Keil and Alex Yu, Matthew Tancik, Qinlong Chen, Benjamin Recht, and Angjoo Kanazawa. Plenoxels: Radiance fields without neural networks. In *CVPR*, 2022.
- [38] Johannes Lutz Schönberger and Jan-Michael Frahm. Structure-from-motion revisited. In *CVPR*, 2016.
- [39] Johannes Lutz Schönberger, Enliang Zheng, Marc Pollefeys, and Jan-Michael Frahm. Pixelwise view selection for unstructured multi-view stereo. In *ECCV*, 2016.
- [40] Soshi Shimada, Vladislav Golyanik, Christian Theobalt, and Didier Stricker. Ismo-gan: Adversarial learning for monocular non-rigid 3d reconstruction. In *CVPRW*, 2019.
- [41] Vikramjit Sidhu, Edgar Tretschk, Vladislav Golyanik, Antonio Agudo, and Christian Theobalt. Neural dense non-rigid structure from motion with latent space constraints. In *ECCV*, 2020.
- [42] Miroslava Slavcheva, Maximilian Baust, Daniel Cremers, and Slobodan Ilic. Killingfusion: Non-rigid 3d reconstruction without correspondences. In *CVPR*, pages 1386–1395, 2017.
- [43] Cheng Sun, Min Sun, and Hwann-Tzong Chen. Direct voxel grid optimization: Super-fast convergence for radiance fields reconstruction. In *CVPR*, pages 5459–5469, 2022.
- [44] Ayush Tewari, Justus Thies, Ben Mildenhall, Pratul Srinivasan, Edgar Tretschk, Wang Yifan, Christoph Lassner, Vincent Sitzmann, Ricardo Martin-Brualla, Stephen Lombardi, Tomas Simon, Christian Theobalt, Matthias Nießner, Jonathan T. Barron, Gordon Wetzstein, Michael Zollhöfer, and Vladislav Golyanik. Advances in Neural Rendering. *Comput. Graph. Forum*, 2022.
- [45] Edgar Tretschk, Ayush Tewari, Vladislav Golyanik, Michael Zollhöfer, Christoph Lassner, and Christian Theobalt. Non-rigid neural radiance fields: Reconstruction and novel view synthesis of a dynamic scene from monocular video. In *ICCV*, pages 12959–12970, 2021.
- [46] Chaoyang Wang, Xueqian Li, Jhony Kaesemodel Pontes, and Simon Lucey. Neural prior for trajectory estimation. In *CVPR*, 2022.
- [47] Liao Wang, Jiakai Zhang, Xinhang Liu, Fuqiang Zhao, Yan-shun Zhang, Yingliang Zhang, Minye Wu, Jingyi Yu, and Lan Xu. Fourier plenotrees for dynamic radiance field rendering in real-time. In *CVPR*, pages 13524–13534, 2022.
- [48] Zhou Wang, Alan C Bovik, Hamid R Sheikh, and Eero P Simoncelli. Image quality assessment: from error visibility to structural similarity. *IEEE TIP*, 13(4):600–612, 2004.
- [49] Tianhao Wu, Fangcheng Zhong, Andrea Tagliasacchi, Forrester Cole, and Cengiz Oztireli. D<sup>2</sup>NeRF: Self-supervised decoupling of dynamic and static objects from a monocular video. *arXiv preprint arXiv:2205.15838*, 2022.
- [50] Wenqi Xian, Jia-Bin Huang, Johannes Kopf, and Changil Kim. Space-time neural irradiance fields for free-viewpoint video. In *CVPR*, pages 9421–9431, 2021.
- [51] Alex Yu, Ruilong Li, Matthew Tancik, Hao Li, Ren Ng, and Angjoo Kanazawa. Plenotrees for real-time rendering of neural radiance fields. In *ICCV*, pages 5752–5761, 2021.
- [52] Alex Yu, Vickie Ye, Matthew Tancik, and Angjoo Kanazawa. pixelnerf: Neural radiance fields from one or few images. In *CVPR*, pages 4578–4587, 2021.
- [53] Jiakai Zhang, Liao Wang, Xinhang Liu, Fuqiang Zhao, Minzhang Li, Haizhao Dai, Boyuan Zhang, Wei Yang, Lan Xu, and Jingyi Yu. Neuvv: Neural volumetric videos with immersive rendering and editing. *arXiv preprint arXiv:2202.06088*, 2022.
- [54] Kai Zhang, Gernot Riegler, Noah Snavely, and Vladlen Koltun. Nerf++: Analyzing and improving neural radiance fields. *arXiv preprint arXiv:2010.07492*, 2020.
- [55] Richard Zhang, Phillip Isola, Alexei A Efros, Eli Shechtman, and Oliver Wang. The unreasonable effectiveness of deep features as a perceptual metric. In *CVPR*, pages 586–595, 2018.



### Full Body Recording Setup



### Portrait Videos Recording Setup



**Figure 8. Multi-view recording setups for the MMVA dataset.** (Left): The setup used for the full-body recordings; (Right): the setup for the facial performances.

## Supplementary Material

This supplementary document provides more details on our new *MMVA* dataset (Sec. A), along with additional comparisons between the proposed *MoNeRF* and the benchmark methods examined in the main paper (Sec. B).

### A. The MMVA Dataset

The main goal of our MMVA dataset is to investigate the adaptability of monocularized data (in the spirit of the established D-NeRF dataset [33]) to real-world scenarios. On top, it can serve as a benchmark for developing and evaluating new methods tailored towards fast full 360° inward-facing reconstruction from monocular sequences, which is currently limited to synthetic scenes.

The synthetic D-NeRF dataset consists of eight sequences showing deforming objects rendered from a single view per time-frame from a camera position randomly sampled from the full upper hemisphere. For dynamic scenes, this setup entails various benefits over continuous camera recordings. Most importantly, the rapidly changing viewing angles of the teleporting cameras allow observing adjacent deformation states from varying perspectives, enabling high-quality full 360° novel view synthesis over the entire temporal sequence. At the same time, the image sequences remain small in size (*i.e.*, the same as a monocular recording of the same length), meaning they can be pre-loaded into GPU VRAM for fast and efficient training.

When creating our MMVA dataset, we closely follow the D-NeRF dataset specifications to maintain comparability and compatibility with recent methods. As continuous sampling is impossible for real-world setups, and we want to avoid motion blur from fast-moving cameras, we record our dataset using a large-scale synchronized multi-view setup; see Fig. 8. We then monocularize the multi-view data by selecting a single camera image per timeframe for training, *i.e.*, a discrete version of the D-NeRF hemi-

sphere sampling. Using this setup, we record a total of twelve (*i.e.*, ten full-body and two face) sequences showing human actors performing different actions in a variety of challenging clothing. Like the D-NeRF sequences, our recordings contain single short motions (100-250 frames, 2-5 seconds). A visualization of all our sequences is available in our supplemental video. We calibrate the cameras using COLMAP [38, 39] and extract foreground masks via background subtraction and human body segmentation. We then re-scale the camera extrinsics such that the actor is located at a zero-centered cube of side 0.5. The final data format is designed to be compatible with existing NeRF implementations and only adds per-camera focal lengths and principal points. The full dataset is available at our project page.

### B. Additional Results

In this section, we report an additional experiment to compare our method’s capabilities against the most related static InstantNGP [24], and provide detailed per-scene results for the experiments in the main document.

#### B.1. Comparison to InstantNGP

To investigate the difference in quality to its static counterpart, we compare our MoNeRF to the neural radiance field implementation of InstantNGP [24]. To this end, we train InstantNGP on one static frame of our MMVA Plush-Dog sequence. In contrast to MoNeRF, which is trained on the entire monocular sequence (*i.e.*, only sees one single image per timeframe), we leverage the multi-view recordings of our MMVA dataset to train instantNGP on all 107 camera views of a single timeframe in the middle of the sequence. Figure 9 shows renderings from a novel view unseen by both methods during training. We observe that our MoNeRF produces more blur in dynamic image regions, like the plush dog and the actor’s face, as it has to jointly infer the scene motion and appearance from a single image at a time. InstantNGP, on the other hand, when provided with multi-

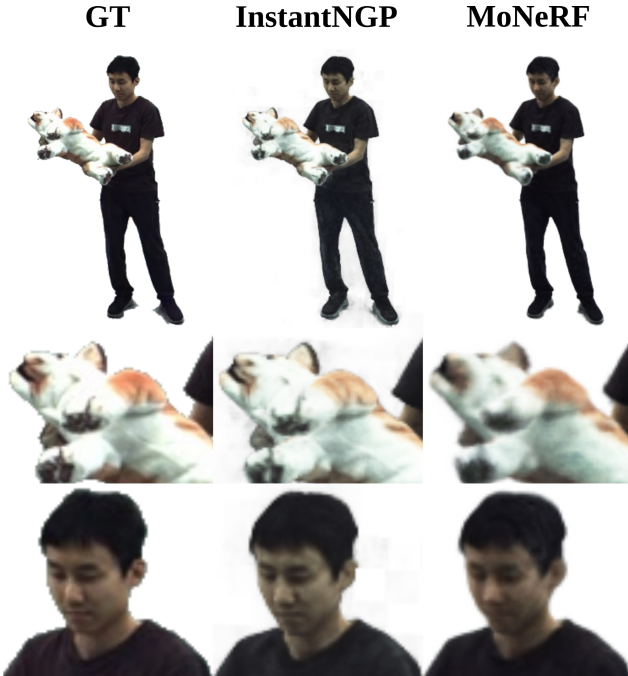


**Figure 9. Comparison on a single static frame:** A novel view generated by InstantNGP [24] and our MoNeRF. While our method was trained on the monocularized dynamic sequence, InstantNGP was provided with 107 multi-view images for the static frame. MoNeRF produces more blurry results in deforming areas of the scene but still maintains an overall high image quality.

view data, can reconstruct fine details for the entire static frame. However, when provided with monocularized data of a dynamic scene, the static architecture of InstantNGP cannot reconstruct a consistent representation of the scene, as shown in our detailed comparisons below (see Fig. 11).

Despite the drastically reduced training data per time frame and additional task of compensating dynamic scene deformations, our MoNeRF is capable of visually appealing novel view synthesis close to the quality of related static multi-view approaches.

## B.2. Depth Map Reconstruction

The main goal of our MoNeRF approach is high-fidelity free 360° spatiotemporal novel view synthesis for non-rigidly deforming scenes. To generate the final RGB output images, the underlying ray-marching-based volume rendering from a neural radiance field reconstructs an implicit 3D model, which enables the extraction of dense metrical depth maps or explicit scene geometry. While reconstructing static geometry from multiple calibrated input views is a well-constrained problem, estimating a temporally consistent representation from monocular recordings of a dynamic scene is far more challenging. In Fig. 10, we show examples of depth maps generated by MoNeRF when rendering

novel views for all scenes from the D-NeRF and MMVA datasets. As can be seen, our method is not only capable of rendering visually appealing RGB images but also faithfully reconstructs consistent 3D information over the entire temporal sequence.

## B.3. Detailed Comparisons

In the main paper, we compare MoNeRF to two benchmark methods, namely D-NeRF [33] and NR-NeRF [45]. In Tab. 4 and Tab. 5, we supplement our experiments with detailed per-sequence quantitative analysis for the D-NeRF and MMVA datasets, respectively. We also provide more qualitative comparisons in Fig. 11 and Fig. 12, showing all remaining dataset sequences not contained in the main document. Across all sequences, our method does not only train and render significantly faster than the benchmark methods, but also yields sharper, more detailed textures and object boundaries on a per-image level. We further observe that MoNeRF’s video results are less jittery than those of D-NeRF and NR-NeRF. Recall that due to the monocularized setting with arbitrary sampled camera views, the differences in the input observations can be significant, which leads to the jitter in the deformable scene representations of D-NeRF and NR-NeRF. In contrast, our architecture is especially robust to such artefacts due to the inductive bias of our factorization-based deformation module.

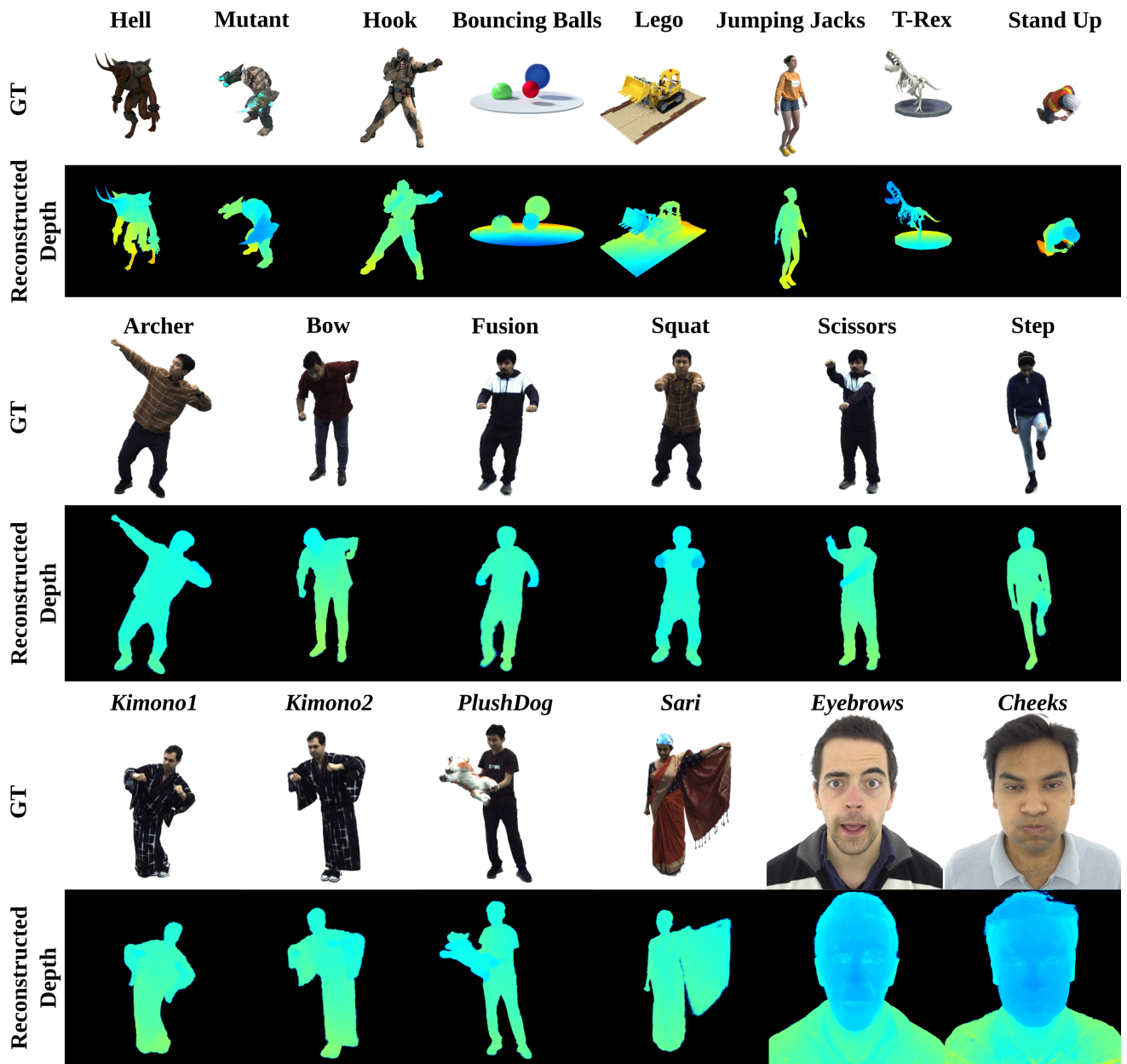


**Figure 10. Depth map reconstruction:** We show ground-truth (GT) images from the test sets of all scenes and the corresponding depth maps reconstructed by MoNeRF and visualized as heatmaps (blue: near; red: far).

Method	<i>Hell Warrior</i>			<i>Mutant</i>			<i>Hook</i>			<i>Bouncing Balls</i>		
	PSNR $\uparrow$	SSIM $\uparrow$	LPIPS $\downarrow$	PSNR $\uparrow$	SSIM $\uparrow$	LPIPS $\downarrow$	PSNR $\uparrow$	SSIM $\uparrow$	LPIPS $\downarrow$	PSNR $\uparrow$	SSIM $\uparrow$	LPIPS $\downarrow$
NERF [23]	13.52	0.81	0.25	20.31	0.91	0.09	16.65	0.84	0.19	20.26	0.91	0.20
DirectVoxGO [43]	13.32	0.75	0.25	19.45	0.89	0.12	16.16	0.80	0.21	20.20	0.87	0.22
Plenoxels [37]	15.19	0.78	0.27	21.44	0.91	0.09	17.90	0.81	0.21	21.30	0.89	0.18
InstantNGP [24]	15.28	0.84	0.26	20.59	0.91	0.11	15.92	0.82	0.23	19.12	0.89	0.19
T-NeRF [33]	23.19	0.93	0.08	30.56	0.96	0.04	27.21	0.94	0.06	37.81	0.98	0.12
D-NeRF [33]	25.02	0.95	<b>0.06</b>	31.29	0.97	0.02	29.25	0.96	0.11	38.93	0.98	0.10
NR-NeRF [45]	23.74	0.94	0.07	30.77	0.97	0.03	26.49	0.94	0.07	24.72	0.95	0.15
<b>MoNeRF</b>	<b>26.53</b>	<b>0.96</b>	<b>0.06</b>	<b>35.51</b>	<b>0.99</b>	<b>0.01</b>	<b>31.12</b>	<b>0.98</b>	<b>0.03</b>	<b>39.45</b>	<b>0.99</b>	<b>0.04</b>
TiNeuVox-S [7]	27.00	0.95	0.09	31.09	0.96	0.05	29.30	0.95	0.07	39.05	0.99	0.06
TiNeuVox-B [7]	28.17	0.97	0.07	33.61	0.98	0.03	31.45	0.97	0.05	40.73	0.99	0.04
NDVG [11]	25.53	0.95	0.07	35.53	0.99	0.01	29.80	0.96	0.04	34.58	0.97	0.11

Method	<i>Lego</i>			<i>T-Rex</i>			<i>Stand Up</i>			<i>Jumping Jacks</i>		
	PSNR $\uparrow$	SSIM $\uparrow$	LPIPS $\downarrow$	PSNR $\uparrow$	SSIM $\uparrow$	LPIPS $\downarrow$	PSNR $\uparrow$	SSIM $\uparrow$	LPIPS $\downarrow$	PSNR $\uparrow$	SSIM $\uparrow$	LPIPS $\downarrow$
NERF [23]	20.30	0.79	0.23	24.49	0.93	0.13	18.19	0.89	0.14	18.28	0.88	0.23
DirectVoxGO [43]	21.13	0.90	0.10	23.27	0.92	0.09	17.58	0.86	0.16	17.80	0.84	0.20
Plenoxels [37]	21.97	0.90	0.11	25.18	0.93	0.08	18.76	0.87	0.15	20.18	0.86	0.19
InstantNGP [24]	19.99	0.90	0.11	25.45	0.94	0.07	15.99	0.86	0.20	19.62	0.90	0.17
T-NeRF [33]	23.82	0.90	0.15	30.19	0.96	0.13	31.24	0.97	0.02	32.01	0.97	<b>0.03</b>
D-NeRF [33]	21.64	0.83	0.16	31.75	0.97	0.03	32.79	0.98	0.02	<b>32.80</b>	<b>0.98</b>	<b>0.03</b>
NR-NeRF [45]	23.90	0.91	0.14	28.28	0.96	0.12	26.61	0.96	0.05	24.70	0.94	0.09
<b>MoNeRF</b>	<b>25.19</b>	<b>0.94</b>	<b>0.04</b>	<b>33.06</b>	<b>0.99</b>	<b>0.02</b>	<b>34.29</b>	<b>0.99</b>	<b>0.01</b>	32.14	<b>0.98</b>	<b>0.03</b>
TiNeuVox-S [7]	24.35	0.88	0.13	29.95	0.96	0.06	32.89	0.98	0.03	32.33	0.97	0.04
TiNeuVox-B [7]	25.02	0.92	0.07	32.70	0.98	0.03	35.43	0.99	0.02	34.23	0.98	0.03
NDVG [11]	25.23	0.93	0.05	30.15	0.97	0.05	34.05	0.98	0.02	29.45	0.96	0.08

**Table 4. Quantitative per-scene comparison on the D-NeRF [33] dataset.** We report PSNR/SSIM (higher is better) and LPIPS (lower is better) for all eight dynamic scenes of the D-NeRF dataset. The best results are highlighted in bold. We highlight occasional better results in italics for concurrent work (last three rows).

Method	<i>Archer</i>			<i>Bow</i>			<i>Cheeks</i>			<i>Eyebrows</i>		
	PSNR $\uparrow$	SSIM $\uparrow$	LPIPS $\downarrow$	PSNR $\uparrow$	SSIM $\uparrow$	LPIPS $\downarrow$	PSNR $\uparrow$	SSIM $\uparrow$	LPIPS $\downarrow$	PSNR $\uparrow$	SSIM $\uparrow$	LPIPS $\downarrow$
InstantNGP [24]	14.77	0.89	0.29	14.48	0.88	0.24	23.86	0.86	0.17	19.96	0.83	0.19
D-NeRF [33]	32.41	<b>0.99</b>	0.02	35.07	0.99	0.06	27.56	0.89	0.20	26.68	0.91	0.23
NR-NeRF [45]	30.50	0.98	0.02	30.24	0.99	0.02	<b>27.70</b>	0.89	0.18	<b>27.24</b>	0.91	0.15
<b>MoNeRF</b>	<b>34.57</b>	<b>0.99</b>	<b>0.01</b>	<b>37.18</b>	<b>1.00</b>	<b>0.01</b>	27.18	<b>0.90</b>	<b>0.13</b>	26.93	<b>0.92</b>	<b>0.11</b>

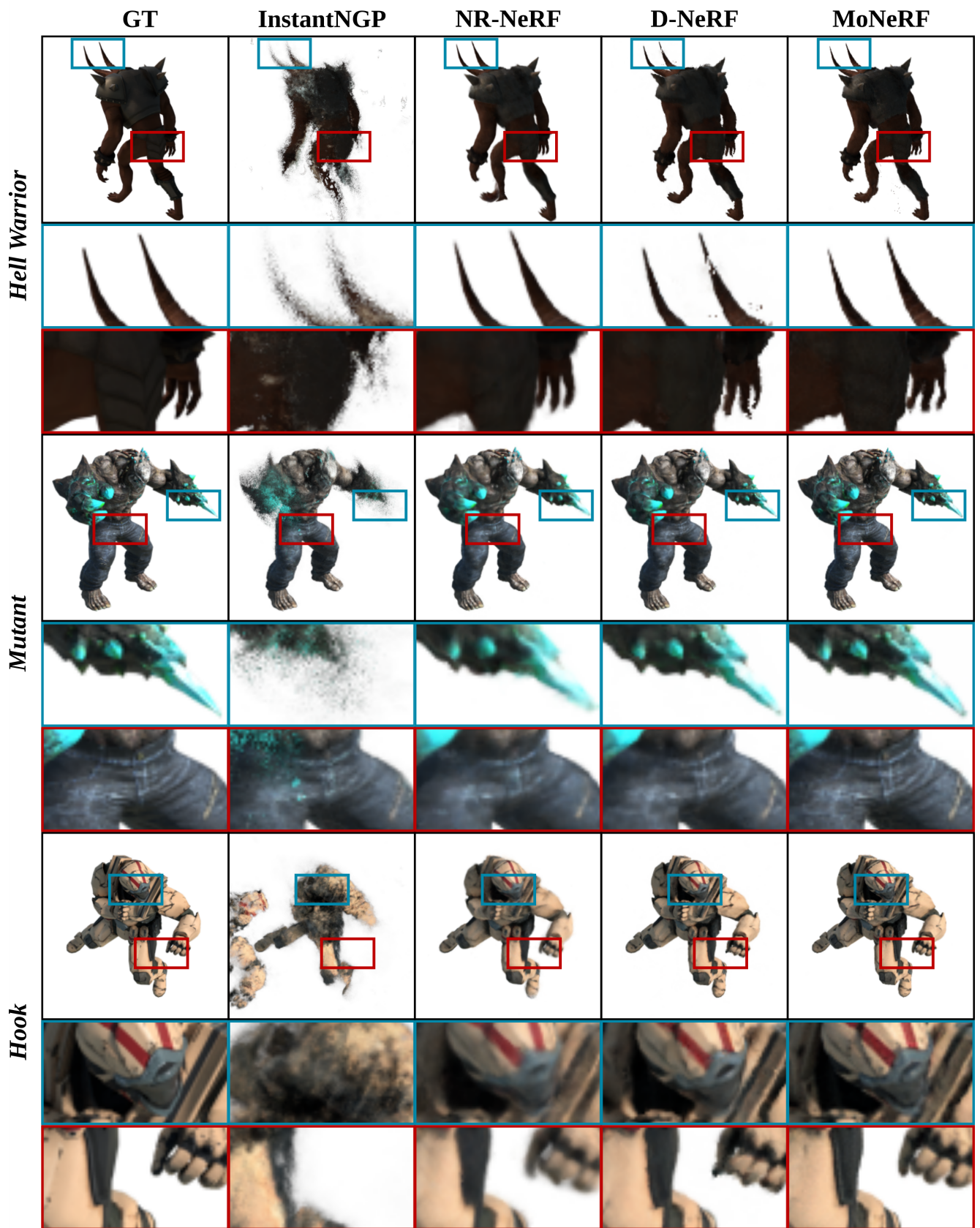
Method	<i>Fusion</i>			<i>Kimono1</i>			<i>Kimono2</i>			<i>PlushDog</i>		
	PSNR $\uparrow$	SSIM $\uparrow$	LPIPS $\downarrow$	PSNR $\uparrow$	SSIM $\uparrow$	LPIPS $\downarrow$	PSNR $\uparrow$	SSIM $\uparrow$	LPIPS $\downarrow$	PSNR $\uparrow$	SSIM $\uparrow$	LPIPS $\downarrow$
InstantNGP [24]	16.13	0.93	0.16	12.16	0.89	0.59	15.13	0.91	0.31	15.70	0.89	0.30
D-NeRF [33]	32.83	<b>0.99</b>	0.14	30.80	<b>0.98</b>	0.13	30.33	<b>0.98</b>	<b>0.02</b>	29.62	0.98	0.02
NR-NeRF [45]	30.80	<b>0.99</b>	0.02	29.09	<b>0.98</b>	<b>0.02</b>	28.97	<b>0.98</b>	<b>0.02</b>	29.50	0.98	0.03
<b>MoNeRF</b>	<b>34.32</b>	<b>0.99</b>	<b>0.01</b>	<b>31.39</b>	<b>0.98</b>	<b>0.02</b>	<b>31.29</b>	<b>0.98</b>	<b>0.02</b>	<b>35.67</b>	<b>0.99</b>	<b>0.01</b>

Method	<i>Sari</i>			<i>Scissors</i>			<i>Squat</i>			<i>Step</i>		
	PSNR $\uparrow$	SSIM $\uparrow$	LPIPS $\downarrow$	PSNR $\uparrow$	SSIM $\uparrow$	LPIPS $\downarrow$	PSNR $\uparrow$	SSIM $\uparrow$	LPIPS $\downarrow$	PSNR $\uparrow$	SSIM $\uparrow$	LPIPS $\downarrow$
InstantNGP [24]	14.28	0.90	0.36	15.52	0.93	0.20	13.73	0.90	0.53	16.73	0.94	0.27
D-NeRF [33]	32.80	0.98	0.07	35.21	0.99	<b>0.01</b>	32.80	<b>0.99</b>	0.02	35.07	0.99	<b>0.01</b>
NR-NeRF [45]	29.66	0.98	0.03	31.36	0.99	<b>0.01</b>	31.97	<b>0.99</b>	0.02	31.02	0.99	<b>0.01</b>
<b>MoNeRF</b>	<b>33.50</b>	<b>0.99</b>	<b>0.01</b>	<b>36.52</b>	<b>1.00</b>	<b>0.01</b>	<b>34.62</b>	<b>0.99</b>	<b>0.01</b>	<b>36.26</b>	<b>1.00</b>	<b>0.01</b>

**Table 5. Quantitative per-scene comparison on our MMVA dataset.** We report PSNR/SSIM (higher is better) and LPIPS (lower is better) on all twelve dynamic scenes of our dataset. The best results are highlighted in bold.





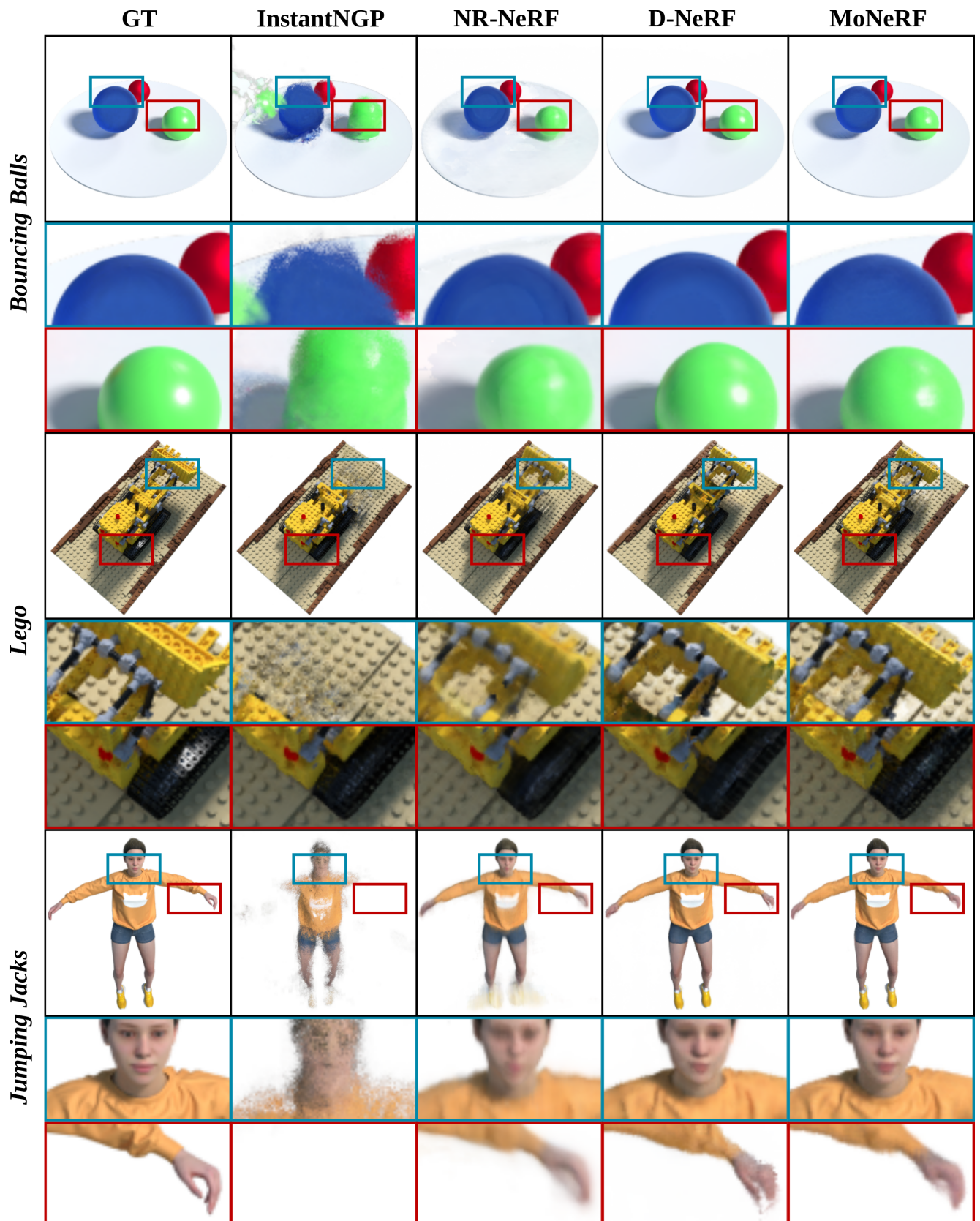


Figure 11. Qualitative comparisons on the D-NeRF [33] dataset: Novel view synthesis on the remaining six scenes.

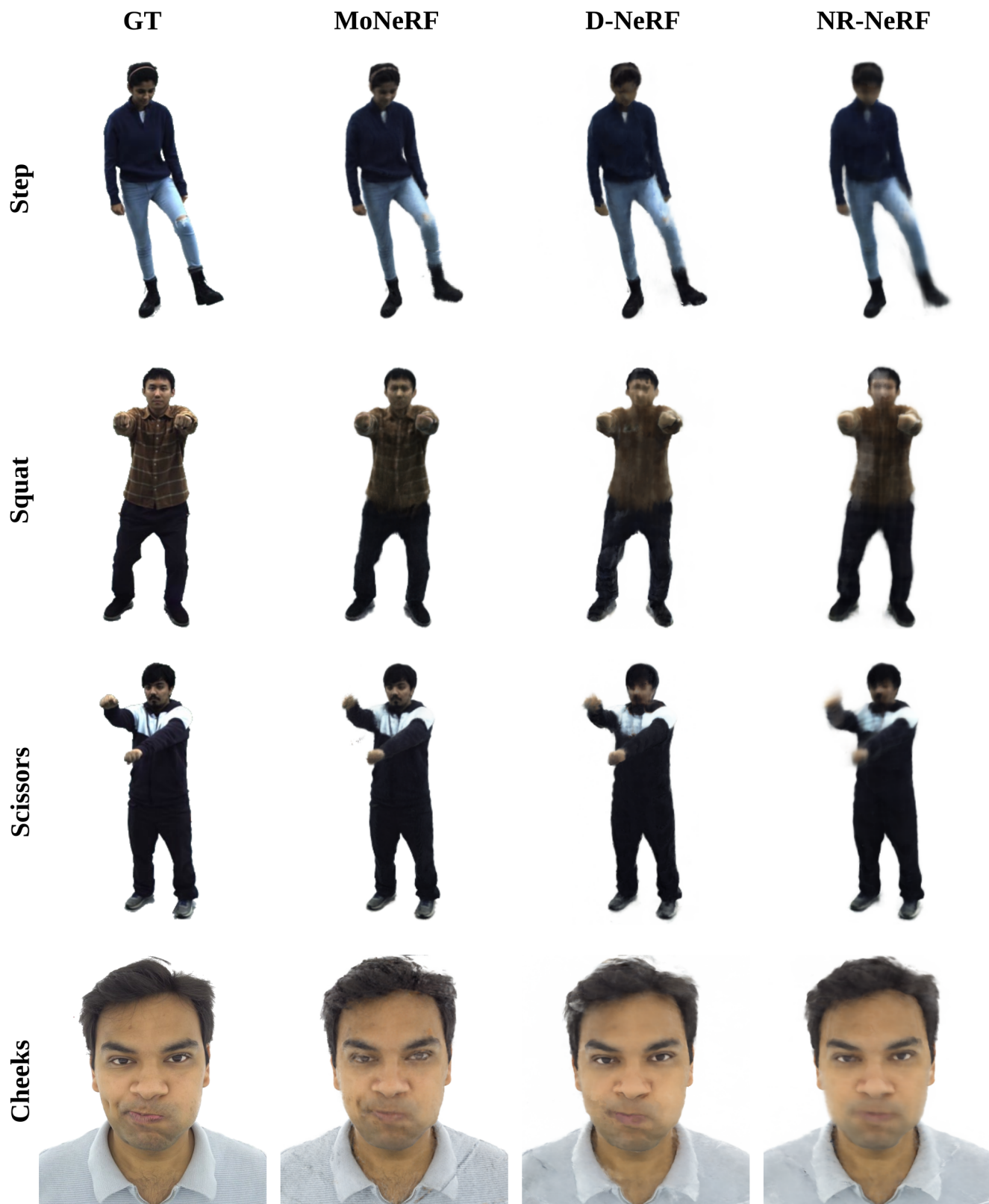


Figure 12. Further qualitative comparisons on our MMVA dataset: Novel view synthesis on the remaining four scenes.